Ore Geology Reviews 106 (2019) 192–204

Contents lists available at ScienceDirect

Ore Geology Reviews

journal homepage: www.elsevier.com/locate/oregeorev

Ferro-manganese nodules from the Kara Sea: Mineralogy, geochemistry and genesis

Oleg S. Vereshchagin[a,*], Elena N. Perova[a], Aleksey I. Brusnitsyn[a], Victoria B. Ershova[a], Andrey K. Khudoley[a], Vladimir V. Shilovskikh[b], Elena V. Molchanova[c]

[a] Institute of Earth Sciences, Saint Petersburg State University, Russia
[b] Geomodel Resource Center, Saint Petersburg State University, Russia
[c] Polar Marine Geosurvey Expedition, Russia

ARTICLE INFO

Keywords:
Ferromanganese nodule
Ferromanganese mineralization
Nodules
Kara Sea
Birnessite
Buserite
Classification

ABSTRACT

Sixteen ferromanganese nodules collected from a large area in the Kara Sea were studied by optical and scanning electron microscopy, X-ray powder diffraction, X-ray fluorescence analysis, inductively coupled plasma mass spectrometry, and electron microprobe analysis. The geological setting, chemical and mineralogical features suggest that Fe-Mn concretions of the Kara Sea mainly were formed by diagenetic process, while hydrogenetic process is secondary if present. The studied nodules are characterized by the alternation of Mn- and Fe-P-enriched laminae. The Fe-P-rich laminae are almost completely composed of an amorphous phase under X-ray. We consider that the phosphatization process did not occur during formation of the Fe-Mn crusts and nodules from the Kara Sea. Several Mn-bearing phases are present in the studied samples (buserite-1, birnessite and X-ray amorphous phase). All studied nodules have similar contents of the main chemical elements. In all cases, the samples are depleted in light REE, enriched in heavy REE, and have negative Ce and Y anomalies. Our data indicate that diagenetic crusts and nodules differ significantly in terms of chemical composition from other types of Fe-Mn concretions. Based on their Co, Ni, Cu, Ce, Zr and Mo contents, we could differentiate diagenetic concretions from hydrogenetic and hydrothermal (both high and low-temperature) concretions.

1. Introduction

Ferromanganese nodules and crusts (hereafter called Fe-Mn concretions) were first discovered in the Kara Sea in 1878–1880 by the expedition of A.E. Nordenskjold (Nordenskjold, 1881), but received no further study for almost a century. Since the middle of the 20th century, interest in the study of Fe-Mn concretions has increased significantly, due to their ubiquitous occurrence in the World Ocean (Bonatti et al., 1972; Calvert and Price, 1977; Aplin and Cronan, 1985; Halbach and Puteanus, 1988; Cherkashov et al., 2017; Konstantinova et al., 2017), and also the discovery of Mn-enriched hydrothermal mineralization (Hein et al., 1997, 2008a,b). More recently, Fe-Mn concretions have emerged as promising host deposits for polymetallic and rare earth element ores, therefore their study has received heightened interest from an economic perspective (e.g. Bau et al., 1996; Hein et al., 2013; Hein and Koschinsky, 2013).

The variety of genetic types of Fe-Mn concretions from modern seas and oceans and their spatial distribution are considered in a series of reviews (Bonatti et al., 1972; Halbach and Puteanus, 1988; Hein et al., 1997; Hein and Koschinsky, 2013; Bau et al., 2014; Josso et al., 2017). Based on the geological settings and chemical composition of Fe-Mn concretions, they can be subdivided into three main groups: hydrothermal, hydrogenetic and diagenetic (Bonatti et al., 1972; Hein et al., 1997; Bau et al., 2014; Josso et al., 2017).

Hydrothermal concretions are formed by precipitation of Mn- and/or Fe oxyhydroxides from hydrothermal fluids (Hein et al., 2008a,b). The growth rate of hydrothermal crusts and nodules is relatively fast and in some cases reaches a rate of ~ 100 mm per million years (e.g. González et al., 2012). Since hydrothermal crusts and nodules could be formed under various conditions and temperature (e.g. Bonatti, 1975; Hein et al., 2008a,b; Josso et al., 2017), the trace metals content and Mn/Fe ratio can vary significantly (e.g. Josso et al., 2017; Kuhn et al., 2017).

Hydrogenetic concretions are formed by direct precipitation of colloidal hydrous metal oxides from oceanic water onto the solid substrate (volcanic or sedimentary rocks) in the anoxic zone, which approximate depths of 1–2 km (Koschinsky and Halbach, 1995; Bau et al., 1996; Koschinsky and Hein, 2003; Asavin et al., 2010; Kuhn et al.,

* Corresponding author.
E-mail address: o.vereshchagin@spbu.ru (O.S. Vereshchagin).

https://doi.org/10.1016/j.oregeorev.2019.01.023
Received 18 September 2018; Received in revised form 20 January 2019; Accepted 25 January 2019
Available online 29 January 2019
0169-1368/

2017). The growth rate of hydrogenetic layers is extremely slow and typically of 1–6 mm per million years (Bau et al., 1996; Koschinsky and Hein, 2003). Generally, hydrogenetic crusts from the global ocean are strongly enriched in Co and Ni, and to a lesser extent in Cu (e.g. Anikeeva et al., 2002; Hein and Koschinsky, 2013) and typically have Mn/Fe ratios ≤5 (Halbach and Puteanus, 1988).

Diagenetic concretions are formed as a result of element precipitation from suboxic pore water and their grow rate is considerably faster – up to 250 mm per million years (Burns and Burns, 1978; Hein and Koschinsky, 2013; von Stackelberg, 2000). Typical elements enriched in diagenetic nodules are Ni, Cu, Ba, Zn, Mo, Li, and Ga (e.g. von Stackelberg, 1997; Kuhn et al., 2017); they have Mn/Fe ratios ≥5 (Halbach and Puteanus, 1988).

Numerous studies have shown that in most cases Fe-Mn concretions from modern seas and oceans have mixed nature. Hydrogenic and hydrothermal crusts can be altered as a result of diagenetic process. Hydrothermal and diagenetic processes do not exclude the possibility of hydrogenic sorption of elements from seawater.

The purpose of this work is to investigate the mineralogical, chemical and textural features of Fe-Mn concretions from the Kara Sea and based on that determine their genesis. All collected samples originate from Quaternary deposits in the north-eastern part of the Kara Sea. A few studies on the Fe-Mn nodules of the Kara Sea have been carried out on several samples (Chukhrov et al., 1976; Koshelev, 1984; Gurevich and Yakovlev, 1993; Bogdanov et al., 1994; Baturin, 2011), however do not offer an insight into their mineralogical, chemical and textural variability in this area. Moreover, relationships between the mineralogical composition and distribution of the main and rare-earth elements to the geological settings of Fe-Mn concretions from the Kara Sea, have been poorly studied to date.

2. Geological framework

The Kara Sea shelf comprises one of the broadest continental shelves bounding the Arctic Ocean. Its geology and tectonic evolution were recently summarized by Pease et al. (2014), Drachev (2016) and Faleide et al. (2017). The Kara Sea shelf is sub-divided by the offshore North Siberian Arch into two distinct tectonic domains: the South Kara Basin and the North Kara Basin (Fig. 1). The North Siberian Arch has been recognized and defined based on seismic profiling, and likely links Late Triassic – Early Jurassic deformations in the Taimyr and Pai-Khoi – Novaya Zemlya fold and thrust belts.

The South Kara Basin is located to the south of the North Siberian Arch and represents the offshore continuation of the West Siberian Sedimentary Basin (Drachev, 2016; Faleide et al., 2017). The nature of the basement is poorly constrained by the available data. Seismic studies reveal a series of SW–NE trending grabens in the basement, which have been typically associated with Permo-Triassic extension described from the onshore West Siberian Basin. However, there is indirect evidence for Late Triassic – Early Jurassic deformation of the basement of the South Kara Basin, suggesting that the rifts could be as young as Early Jurassic (Drachev, 2016; Khudoley et al., 2018). The overlying sedimentary cover consists of Mesozoic and Cenozoic terrigenous rocks up to 15–16 km thick.

The North Kara Basin is located to the north of the North Siberian Arch and is underlain by the Kara microcontinent, comprising a latest Neoproterozoic – earliest Cambrian basement (Ershova et al., 2015). The geology of the North Kara Basin is comparatively poorly studied relative to the South Kara Basin, owing to its lower hydrocarbon prospectivity and more remote location from infrastructure, and the offshore geology has been mainly extrapolated from the Severnaya Zemlya archipelago and northern Taimyr. No wells have been drilled here and the stratigraphy of the overlying sedimentary cover is based entirely upon seismic data. A sedimentary infill of up to 12 km is inferred, predominantly composed of Paleozoic carbonate and terrigenous rocks capped with a much thinner succession of Mesozoic terrigenous rocks.

Studies of the mineralogical and chemical compositions of both the modern and Holocene (post Last Glacial Maximum) seafloor sediments show evidence for both glacial and fluvial sediment transport throughout the Kara Sea during this time (Levitan et al., 2004; Lisitsin et al., 2004; Rozanov, 2015; Rusakov et al., 2017). During the Quaternary, major glacio-eustatic sea-level fluctuations strongly controlled the distribution and volume of riverine sediment discharge onto the Kara Sea shelf. Since approximately a half of the modern Kara Sea shelf lies at a water depth of < 100 m, major sea-level regressions during glacial periods allowed fluvial systems to extend hundreds of kilometers northwards onto the Kara Shelf from their present estuaries. However, during the Last Glacial Maximum, the drainage of the Ob and Yenisey rivers was blocked by the southward expansion of vast ice sheets across the Kara Sea shelf and northern Siberia (Polyak et al., 2002).

The highest accumulation rates were recorded in early Holocene in the central Kara Sea when the sea level was about 40–50 m lower than today and large parts of the inner Kara Sea were subaerial (Stein et al., 2004; Hörner et al., 2018). During that time, terrigenous sediments were transported much more to the north from the modern Ob and Yenisey estuaries forming the main depocenter in the central Kara Sea. The modern sea level conditions were established in the southern Kara Sea, approximately 7.5 ka ago (Hörner et al., 2018). With increasing sea level the main depocenter was shifted towards the south and sedimentation in the central Kara Sea was greatly reduced. Towards the north onto the shelf, late Holocene accumulation rates significantly decreased, indicating the decrease in influence of riverine sediment discharge. However, average Holocene values for linear sedimentation rate are quite high throughout the Kara Sea varying from 2 to 45 cm/kyr in the southern and central Kara Sea and from 2 to 32 cm/kyr in the northern Kara Sea (Stein et al., 2004).

3. Samples and analytical methods

3.1. Samples

Samples of Fe-Mn concretions were collected from a large area (Fig. 1) during the expeditions of 2008–2009 and 2014–2015 by the Polar Marine Geological Exploration Expedition (Makariev, 2012). Fe-Mn concretions were found at depths ranging from 43 to 158 m in the Kara Sea (Table 1). In general, Fe-Mn concretions were found on the seafloor at the sediment surface, although occasionally they were found buried up to a depth of 20 cm.

Sixteen concretions (Table 1), represented by different morphological types (Fig. 2), were selected for study. The morphology of the nodules was deduced by optical and scanning electron microscopy (SEM). Each sample was studied by X-ray powder diffraction (XRD) and X-ray fluorescence analysis (XRF), inductively coupled plasma mass spectrometry (ICP MS), and electron microprobe analysis (EMPA). In addition, it was possible to separate the black inner part of samples FN-46 k and FN-54 k and the clayey outer part of samples FN-54 k and FN-56 k, which were studied individually by XRD.

3.2. Analytical methods

3.2.1. X-ray fluorescence and inductively coupled plasma mass spectrometry

The bulk chemical composition of each sample was determined. Samples were ground to a powder (90% of particles ≤ 80 μm) using an agate pestle and mortar. Chemical analyses were carried out at the All Russian Geological Research Institute (VSEGEI) in St. Petersburg. Whole-rock major element concentrations were determined by the XRF method using an ARL 9800 spectrometer. All measured concentrations are significantly above detection limits, with relative standard deviation of laboratory's precision of less than 5%.

Trace elements and rare earth elements were analyzed by Inductively Coupled Plasma–Mass Spectrometry using an Optima

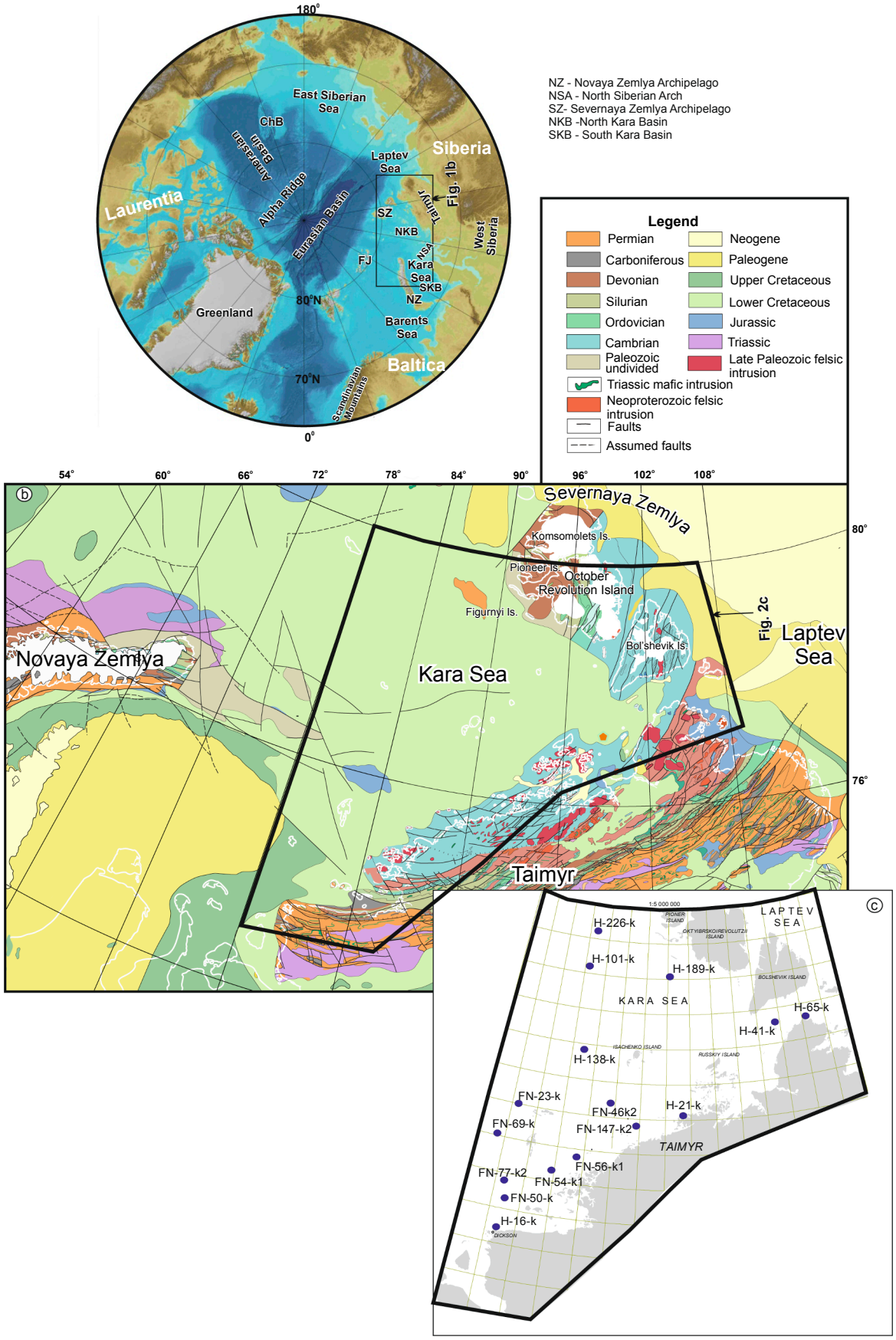

Fig. 1. (a) Map of the Arctic region showing the names and locations mentioned in the figures and text. (b) Simplified geological map of Kara Terrane (from Morozov and Petrov, 2004; Makariev, 2012) with location of studied samples. (c) Sampling locations of ferromanganese nodules from Kara Sea.

Table 1
Description and location of samples analyzed during this study.

No	Sample	Coordinates		Water depth, m	Description
		Latitude	Longitude		
1	FN-23-k	75°59′32,2″N	80°30′16,3″W	54	disk
2	FN-69-k	75° 21′ 45,3″ N	79° 17′ 15,1″W	50	tube
3	FN-50-k	74°11′33,8″N	80°44′21,1″W	50	disk
4	FN-77-k2	74° 31′ 26,1′ N	80° 32′ 15,3″ W.	60	tube
5	FN-54-k1	74°52′48,2″N	83°45′36,4″W	40	spheroidal
6	FN-56-k1	75°12′44,1″N	85°23′58,4″W	46	tube
7	FN-46-k2	75°59′40,8″N	88°14′34,4″W	52	disk
8	FN-147-k2	75° 50′ 31,7″ N	89° 45′ 17,4″ W	41	spheroidal
9	H-138-k	75° 17′ 55,0″N	86° 22′ 28,9″W	63	disk
10	H-189-k	75° 42′ 45,7″N	88° 38′ 30,5″ W	125	disk
11	H-21-k	76° 07′ 0″ N.	93° 13′ 48″ W	43	disk
12	H-16-k	76°16′0″N	87°33′0″W	51	tube
13	H-226-k,t	79° 28′ 58,8″ N	84° 43′ 30″ W	158	disk
14	H-101-k	78° 46′ 30″ N	85° 38′ 30″ W	107	tube
15	H-41-k	77° 43′ 22,8″ N	101° 33′ 29,9″ W	123	tube
16	H-65-k	77° 45′ 18″ N	104° 18′ 18″ W	117	disk

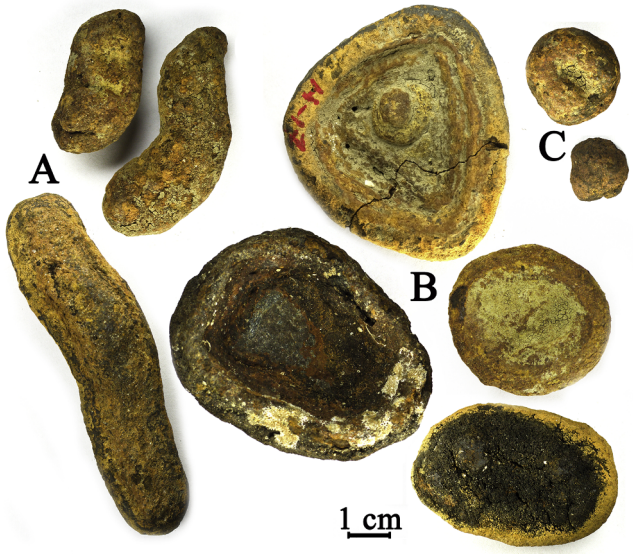

Fig. 2. Photographs of different morphological types of Fe- Mn nodules used in this study: A – tube (H-16-k), B – disk (H-65-k), C – spheroidal (FN-54-k1).

4300DV emission spectrometer and an ELAN 6100 DRC mass spectrometer. All measured concentrations are significantly above detection limits, relative standard deviation of laboratory's precision varying from 4 to 10% for most elements and 15% for Ni. The accuracy of both XRF and ICP-MS analyses was controlled by OU-6 and SBC-1 standards certified by International Association of Geoanalysts and USGS correspondently.

Trace elements and rare earth elements were normalized to Post-Archean Australian Shale (PAAS, Taylor and McLennan, 1985) to calculate the Y/Ho ratio (Bau et al., 2014) and Ce anomaly (Josso et al., 2017).

3.2.2. X-ray powder diffraction

X-ray powder diffraction analysis was carried out at the Research Centre of Saint Petersburg State University for X-ray Diffraction Studies. XRD patterns were recorded using a Rigaku Miniflex II, with a velocity of 2°/min and a step size of 0.02°. Samples of Fe-Mn concretions were studied with Cu K*a* radiation (2-theta range 5–60°), and clay samples with Co k*a* radiation (2-theta range 3–55°). The PDXL II software (Rigaku) was used to identify the mineral phases, accessing The International Centre for Diffraction Data (ICDD) database.

To refine the phase composition of Fe-Mn concretions and to reveal metastable water-containing phases, a series of four X-ray diffraction patterns were taken for each sample following the method proposed by Chukhrov et al. (1976, 1989). Samples were studied at room temperature and after heating in air at 100, 350 and 550 °C. Samples were heated up for 1 h, annealed at the prescribed temperature (100, 350 or 550 °C) for 3 h, and then cooled down to room temperature over a time period of 12 h.

Both clay samples were studied three times by XRD. Clay minerals were separated from quartz and other coarse minerals in two stages. At first, samples were crushed to pass a 63 μm sieve and then filtered through a 0.4 μm filter. Then, the resulting material was re-dispersed in a small amount of purified water and the concentrated suspension was placed on a glass slide and allowed to dry at room temperature (~8 h) to obtain the oriented film. Dried films were used for X-ray powder diffraction. Firstly, air-dried sample was studied. Secondly, the same sample was treated by ethylene glycol to identify smectite group minerals. Finally, the sample was heated (550 °C over 4 h) to identify kaolinite group minerals.

3.2.3. Scanning electron microscopy with energy-dispersive x-ray microanalysis

Nodules of different morphological types were fractured and carbon coated. Their internal structure was examined by scanning electron microscope using the secondary electron imaging with beam voltage of 20 kV using scanning electron microscope Hitachi S-3400N in "Geomodel" research center of Saint-Petersburg State University.

Samples for element microprobe analysis, back-scatter electron imaging and X-ray mapping were placed in epoxy resin and polished on progressively smaller diamond powders. The elemental composition was analyzed using scanning electron microscope Hitachi S-3400N equipped with Oxford X-Max 20 energy dispersive X-ray spectrometer (EDS) in "Geomodel" research center of Saint-Petersburg State University. Due to the fact that the minerals composing the Fe-Mn nodules contain a large number of pores and up to 25 wt% water in their structure (Chukhrov et al., 1976, Drits et al., 1997), all analyzes were normalized to 100%. The conditions of the experiment were: 20 kV accelerating voltage, 1 nA beam current, and 30 s data-collection time (excluding dead time). All the acquired spectra were processed automatically using Oxford AzTec EDX software's True-Q procedure. Rhodochrosite (Mn), pyrite (Fe, S), cobalt metal (Co), nickel metal (Ni), cuprum metal (Cu), albite (Na), periclase (Mg), corundum (Al), quartz (Si), sylvite (K, Cl), apatite (Ca, P), titanium metal (Ti), zinc metal (Zn), barite (Ba), monazite (Ce), molybdenite (Mo), celestine (Sr), vanadium metal (V) were used as standards.

4. Results

4.1. Morphology and texture

All of the studied morphological types of concretions (Fig. 2) are characterized by a concentric-layered texture, which was generated by fine-scale (0.2–1 mm) interbedding of brown and black laminae. These laminae range from 5 to 20 mm in thickness under optical microscopy. Under the SEM, it could be observed that these laminae are separated into smaller zones ranging in thickness from 2 to 200 μm (Fig. 3). In polished samples rosette-like structures that tend to encapsulate and incorporate sediment particles are commonly present (Figs. 3 and 4a and b).

The most common morphological type (Table 1) is disk-like flattened concretions (length 3.5–7 cm, thickness 2–2.5 cm; Fig. 2). The inner parts of the nodules are often composed of a clay substance or an organogenic material (Ca, P-free and C-rich according to EMPA), with a significant admixture of quartz. The second most abundant type of concretions is represented by worm tubes (length 3–9 cm, diameter 0.5–2 cm; Fig. 2). The inner portion of the tubes can also be filled with

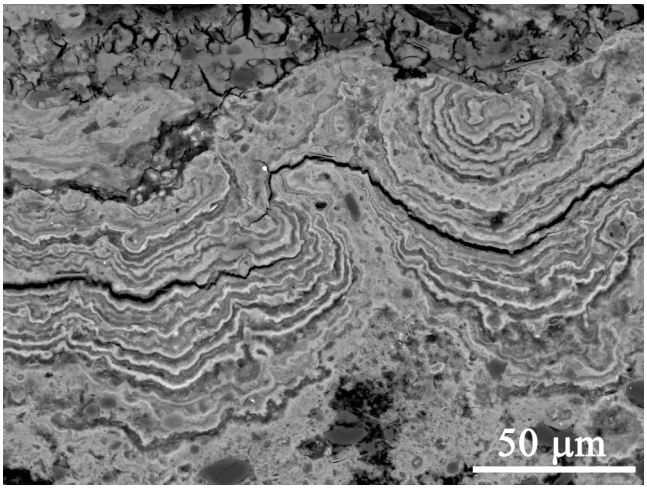

Fig. 3. Growth structures of nodules from the Kara Sea (BSE images). Nanometer thin layers of Fe-, Mn-rich phases (H-101-k).

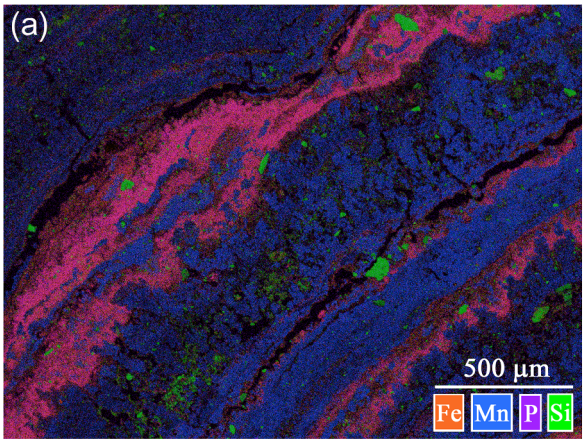

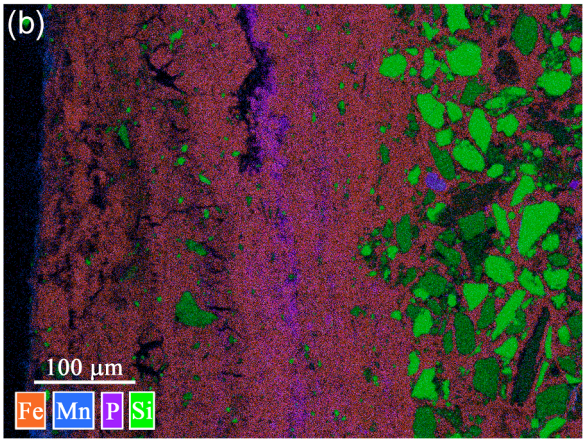

Fig. 4. Elemental maps in FeKα, MnKα, PKα and SiKα of studied samples: a – FN-77-k2, b – H-101-k.

clay or an organic material. Spheroidal nodules (diameter 2–3 cm) are the least common morphological type.

4.2. Mineralogical composition

SEM (Figs. 3 and Fig. 5a–d), XRD (Table 2; Fig. 6a–c) and EMPA (Figs. 4a and b and 7) data indicates the presence of several Mn- or/and

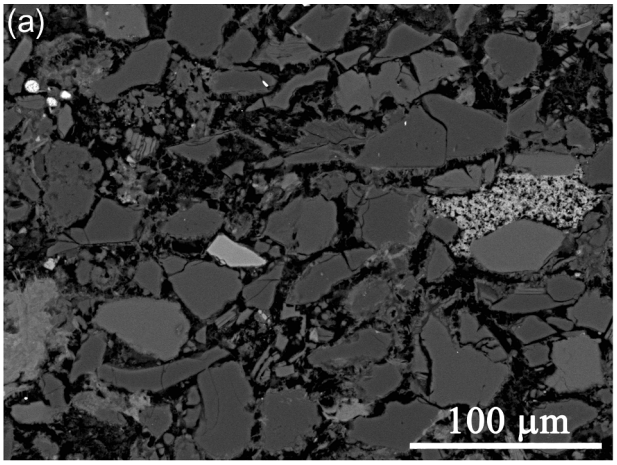

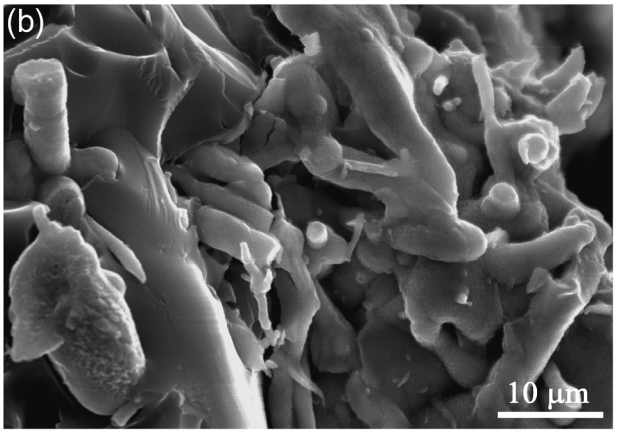

Fig. 5. Morphology of Fe-rich and Mn-rich phases in nodules from the Kara Sea (BSE images): a – framboidal pyrite (bright spots on top left side of the picture) and goethite (mid-gray grains in right side of the picture) in matrix of terrigenous material (H-101-k), b – thin-tube crystals of Fe-bearing Mn-rich phase (H-101-k), c – lamellar crystals of Fe-bearing Mn-rich phase (H-138-k), d – pseudomorph of organic material (?) by Mn-rich phase (FN-46-k2).

Fe-rich phases, which differ in morphology, crystallinity and chemical composition (Fe/Mn ratio, P, Si, Al, Na, Ni contents).

According to XRD, a crystalline Fe-bearing phase, goethite, was found in 1 sample (H-189-k; Table 2); in other cases, brown iron-enriched interlayers are composed of a material which is amorphous under X-ray.

XRD studies (Table 2, Fig. 6a and b) revealed that in all cases the peaks related to manganese-containing phases (10-Å and 7-Å) are disappear at a temperature range of 350–550 °C, which unequivocally indicates the absence of todorokite (Bish and Post, 1989; Post et al., 2003), romanechite, hollandite, cryptomelane and pyrolusite (Bish and Post, 1989).

In nine samples (Table 2), a 10-Å phase was detected, which is most likely represented by buserite-1 (Chukhrov et al., 1976; Manceau et al., 1997; Bilinski et al., 2002). In 14 samples, a 7-Å phase, represented by birnessite, was found. Birnessite is present in all samples containing buserite but also occurs independently, suggesting it formed as a second phase after buserite.

The inner part of sample FN-46 k was completely devoid of terrigenous material, which allowed us to study in detail the thermal behavior of Mn phases (Fig. 6a). After heating in air at 100 °C, the 10-Å phase transformed into the 7-Å phase and peaks disappear at 10 and 4.9 Å, whilst peaks at 7.1 and 3.5 Å were amplified. After a second heating in air at 350 °C, we observe disappearance of the peaks of 7-Å

Table 2
Results of XRD study.

No	Sample	Minerals				
		Mn-bearing				Fe-bearing
		25 °C		100 °C		
		10-Å	7-Å	10-Å	7-Å	Goethite
1	FN-23-k		+		+	
2	FN-69-k					
3	FN-50-k	+	+			
4	FN-77-k2	+	+		+	
5	FN-54-k1-bulk	+	+		+	
6	FN-54-k1-center		+		+	
7	FN-56-k1	+	+		+	
8	FN-46-k2-bulk	+	+		+	
9	FN-46-k2-center	+	+		+	
10	FN-147-k2	+	+		+	
11	H-138-k	+	+		+	
12	H-189-k					+
13	H-21-k	+	+			
14	H-16-k	+	+		+	
15	H-226-k,t		+		+	
16	H-101-k		+		+	
17	H-41-k		+		+	
18	H-65-k		+		+	

phase in the diffractogram. After heating in air at 550 °C (Fig. 6a and b) all (even very small) peaks on diffractogram disappeared.

As many of Mn- and Fe oxides/hydroxides in Fe-Mn concretions have nanometric grain size (e.g. Chukhrov et al., 1976, Drits et al., 1997; Wegorzewski et al., 2015) it is almost impossible to analyze a grain of single mineral by EMPA. Moreover, according to the IMA List of Minerals some of Mn- and Fe oxides/hydroxides common for Fe-Mn concretions have variable water content (e.g. asbolane), unclear chemical formulae (e.g. buserite) or even questionable minerals (e.g. vernadite), which makes almost impossible to calculate chemical formulae of single phase from EMPA. For this reasons the EMPA data for Mn-, Fe-bearing phases were considered as a single set. Detrital material was excluded from the set based on silica and aluminum content (SiO_2 > 30 wt%, Al_2O_3 > 20 wt%) taking into account SEM images. Totally more than 600 EMPA analyses from all studied samples were used to characterize Mn-, Fe-bearing phases.

EMPA data shows (Fig. 7) that there is a continuation between Fe-rich and Mn-rich phases. We assume that such a continuation is a result of nanoscale intergrowth of several Fe, Mn-bearing phases and do not reflect a real isomorphic series. Most of the analysis plot in two separate groups, in the studied samples: either Fe-rich or Mn-rich phases. Fe-rich phases do not contain more than 5 wt% of MnO and Mn-rich phases do not contain more than 15 wt% of Fe_2O_3.

According to EMPA, there are at least three different Fe-rich phases in ferro-manganese nodules from the Kara Sea: goethite, pyrite (Fig. 5a) and amorphous Fe-P phase (Fig. 4a and b). Goethite was found in one sample (H-101-k) as aggregates of small grains (< 1 μm; Fig. 5a) in interstices between detrital grains. Remarkably goethite contain up to 2 wt% of NiO. No over Ni-bearing phases were found in ferro-manganese nodules from the Kara Sea. Framboidal pyrite was found in the same sample (H-101-k) as goethite. The size of framboids does not exceed 5 μm (with crystal size < < 1 μm; Fig. 5a). X-ray amorphous Fe-rich phase have been found in all studied samples. In all cases, phosphorus is associated with iron (Fig. 5b). Low-phosphorus Fe-bearing phase (< 6 wt% P_2O_5) shows strong direct correlation with total iron content ($r^2 \approx 0.7$), while high- phosphorus Fe-bearing phase (6–13 wt% P_2O_5) shows weak correlation with total iron content. Although all the studied samples are P-enriched, no P-bearing crystalline phases were found.

According to EMPA, there are at least two different Mn-rich phases (Fig. 7a). The most Mn-enriched phase (78–87 wt% MnO) is characterized by absence of iron, relatively stable Na and Ca content (5–8 wt% Na_2O, 3–4 wt% CaO), small chlorine content (~1 wt%) and forms fine thin tubular intergrowing aggregates or lamellar crystals (Fig. 5c and d). Another Mn-bearing phase is characterized by high sodium contents (up to 11 wt% Na_2O) and relatively high admixture of iron (up to 15 wt% Fe_2O_3), forming thin-tube crystals (Fig. 5b). Both phases were found in all studied samples.

According to XRD and microprobe analysis data, the clay substance is composed of Mg-Fe-rich chlorite, smectite (nontronite), kaolinite and Mg-Fe-rich mica (Fig. 6c).

The amount of sediment material in Fe-Mn concretions vary significantly in different areas of the same sample (Figs. 3 and 4a and b). Quartz, albite, and feldspars (microcline and plagioclase) were found in all samples and form up to 1/3 of the sample volume (Fig. 4a and b). Quartz grains are of irregular shape and range from 50 to 150 μm in size. Feldspars are characterized by tabular crystals up to 100 μm in size. Ilmenite, magnetite, monazite, zircon, rutile, epidote, Mg-Fe-rich amphibole and chromite were found in subordinate quantities.

4.3. Chemical composition

All of the studied concretions have similar contents of the main chemical elements (Table 3). The nodules show high variability in the Mn/Fe ratio (from ~0.1 to 3.2; Table 3), Al_2O_3 (~10 to 30 wt%) and SiO_2 (~19 to 51 wt%). Other major main elements in the Fe-Mn nodules are much less variable: Na_2O (1.6–3.3 wt%), MgO (1.8–3.0 wt%), K_2O (1.2–2.0 wt%), CaO (0.9–2.4 wt%), TiO_2 (0.2–0.5 wt%). All studied nodules contain a significant amount of phosphorus (more than 1 wt% P_2O_5). In all cases, the loss on ignition is higher than 10 wt%, which indicates the presence of water-containing phases in the nodules.

Co, Ni, and Cu contents (Table 4) are relatively low (Co + Ni + Cu < 400 ppm). EMPA studies reveal that goethite concentrate Ni. No Co- or Cu-bearing phases were found. Other trace elements vary significantly: Sr (179–619 ppm), Y (16–31 ppm), and Zr (13–128 ppm). The studied nodules are characterized by U content of 3–6 ppm which is rather typical for Mn nodules all over the world (Kuhn et al., 2017).

The content of rare-earth elements (REE) is similar in all studied nodules and does not exceed 160 ppm. The PAAS-normalized REE distribution in all nodules is also very similar (Fig. 8). All samples are depleted in light REE and enriched in heavy REE ($HREE_{PAAS}/LREE_{PAAS}$ 3.3–5.0). A negative Ce anomaly was found as well (Ce/Ce* 0.7–0.9). In most nodules (except samples FN-50-k, FN-147 k2, H-21 k, H-41-k, H-65-k), a negative Y anomaly was also identified. The Y_{PAAS}/Ho_{PAAS} ratio varies slightly (0.9–1.1), which indicates that Y/Ho ratio is similar to shale.

The minor and trace elements of the studied Fe-Mn concretions are generally low compared to other hydrothermal and hydrogenetic Fe-Mn nodules and crusts (Kuhn et al., 2017). This is probably due to a significant dilution of the Fe-Mn oxides by detrital phases (mainly by quartz and feldspars). This dilution might also be the reason for the low minor and trace element concentrations. However, such a content of the minor and trace elements is typical for diagenetic concretions from epicontinental seas (e.g. Baturin and Dubinchuk, 2009; Baturin et al., 2011).

5. Discussion

5.1. Genesis

Samples of Fe-Mn concretions were collected over a large geographic area but are characterized by similar mineralogical and geochemical properties, indicating comparable formation conditions. Based on their geological settings Fe-Mn concretions of the Kara Sea (no evidence of recent magmatic and tectonic events in the study region)

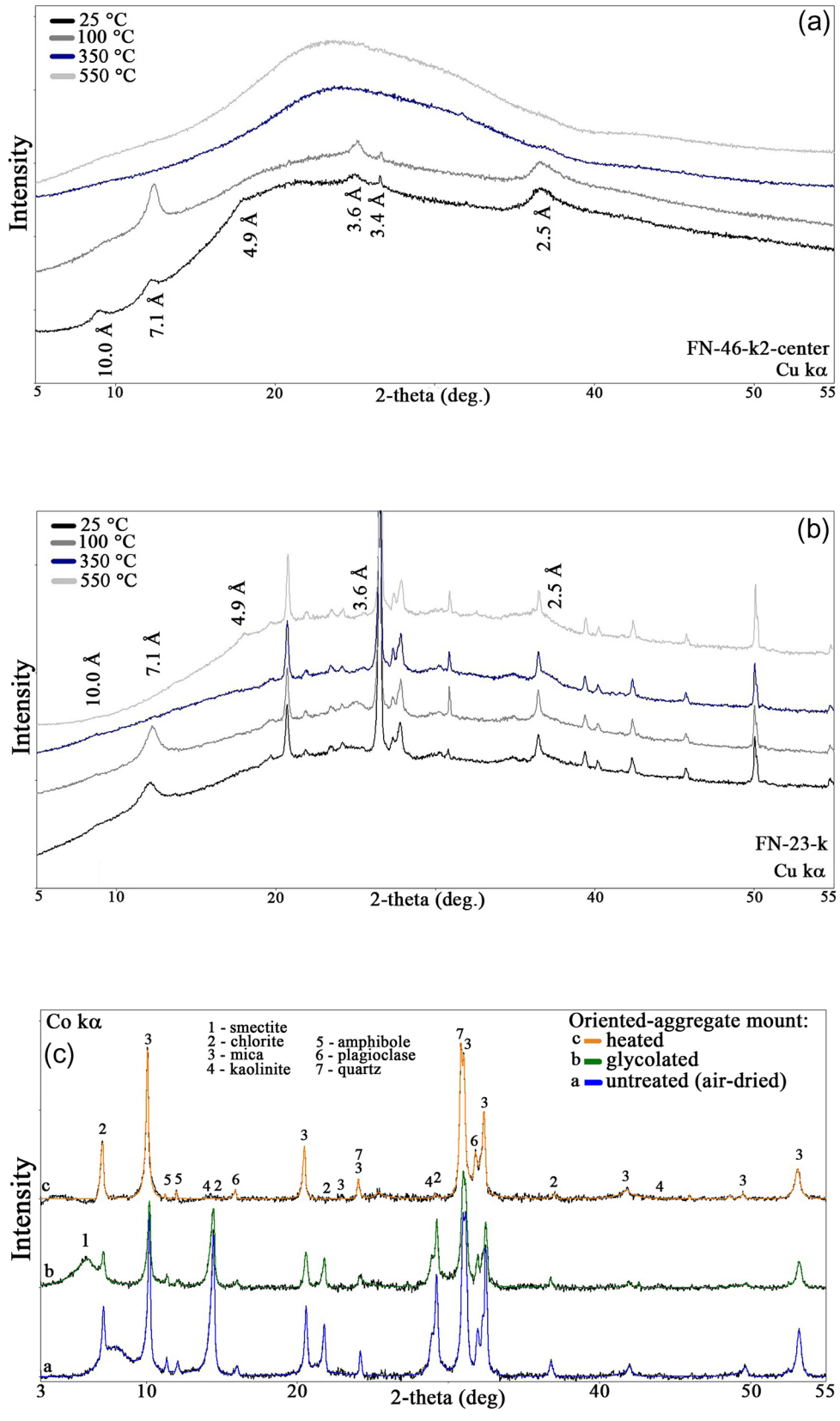

Fig. 6. XRD patterns of studied samples: a - FN-46 k2, b –FN-23-k, c - FN-54-k1.

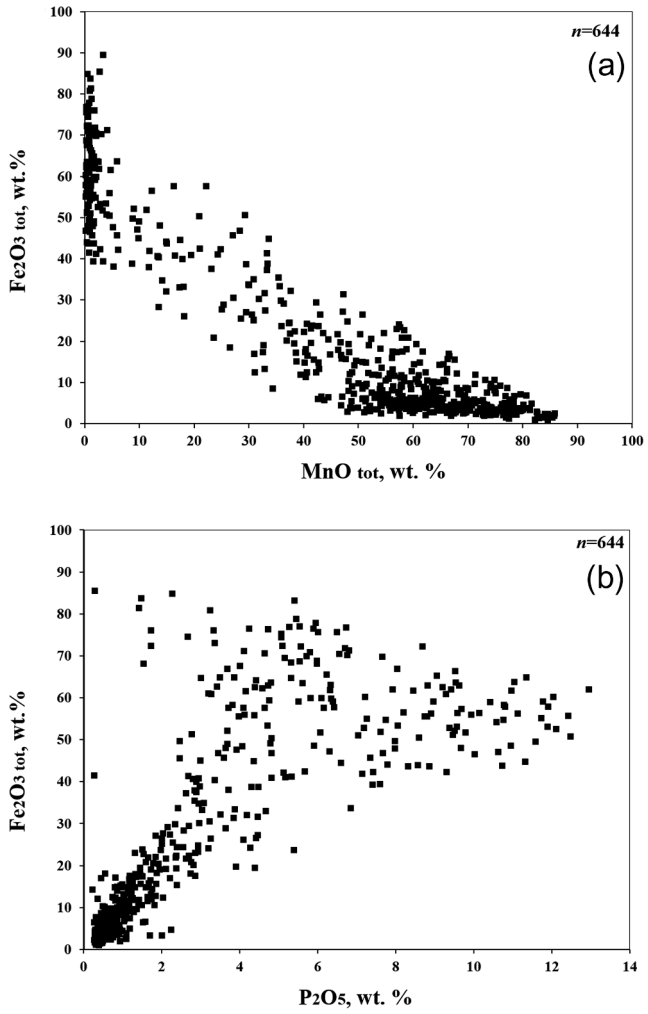

Fig. 7. Chemical variability of Fe-rich and Mn-rich phases: a - MnO_{tot} concentration *vs* Fe_2O_{3tot} concentration; a – P_2O_5 concentration *vs* Fe_2O_{3tot} concentration. Note: *n* - number of EMPA analysis.

should be considered as either diagenetic or hydrogenetic or a mixture of both (Hein et al., 2013).

Hydrogenetic crusts (Fe-Mn crusts) form by direct precipitation of colloidal hydrated metal oxides from the water column onto hard-rock substrates (e.g. Muiños et al., 2013). Sea water is undersaturated by several orders of magnitude by MnO_2 (e.g. Crerar and Barnes, 1974; Baturin, 1988). Therefore, manganese can not precipitated from water onto substrates by itself. Based on that, hydrogenic crusts formation should be limited by specific conditions. It is supposed that oxygen limited layer, which occur in 1–2 km depth and enriched in Mn is one of the main factors controlling their formation (e.g. Emelyanov, 2005). Studied nodules were found in the Kara Sea at the depth of 43–158 m (Table 1). The Kara Sea is relatively well ventilated (e.g. Falkner et al., 2004), which means that no oxygen limited layer is present in this case.

According to Stein et al. (2004) Holocene values for linear sedimentation rate are quite high (> > 2 cm/kyr) throughout the Kara Sea. As Fe-Mn concretions of the Kara Sea were found mostly on the seafloor (and not buried deep into sediments) studied concretions should have relatively (to sedimentation rate) height growing rate.

Most nodules are confined to depths ranging from 40 to 60 m indicating that Fe-Mn concretions of the Kara Sea were formed after Last Glacial Maximum. The size of concretions varies between 0.5 and 7 cm (Fig. 2), which also suggest their height growing rate (> > 100 mm per million years). As growth rate of hydrogenetic layers is extremely slow (typically of 1–6 mm per million years; Bau et al., 1996; Koschinsky and Hein 2003), Fe-Mn concretions of the Kara Sea should be formed mainly by diagenetic process. Very limited influence of hydrogenic factor on formation of Fe-Mn concretions of the Kara Sea might be present.

The mineralogical and textural features of Fe-Mn concretions of the Kara Sea also reflect their formation environment. Internal growth structures of Fe-Mn concretions of the Kara Sea are typical for diagenetic concretions as they have isolated, rosette-like structures (Figs. 3 and 4). The presence of buserite-1 and birnessite is typical for diagenetic concretions. No vernadite (∂-MnO_2) (typical mineral of hydrogenetic concretions; Lei and Boström, 1995) or todorokite (typical mineral of hydrothermal mineral concretions; Burns and Burns, 1978) were found. Our study underscores the importance of studying the thermal behavior of mineral phases to accurately differentiate between the different Fe-Mn concretion groups.

The studied nodules display an alternation of Mn- and Fe-P-enriched laminae (Fig. 4a and b). Two spatially separated mineral associations (Mn-rich and Fe-P-rich) indicates dramatic alternating shifts in the environmental conditions for concentrating ore components in the concretions. According to Bogdanov et al. (1994), the formation of manganese interbeds could occur under low-energy conditions at the seafloor, with silt comprising the upper oxidized layer. Iron-enriched sediments could be formed as the energy levels at the seafloor intensified and mixing of the upper silt layer occurred. This suggests that the Fe oxide phases could be formed by hydrogenetic processes. However, it is difficult to explain relatively big Fe-rich layers (up to 0.5 mm; Fig. 4b) by hydrogenetic processes only as the growth rate of hydrogenetic layers supposed to be extremely slow.

Table 3
Bulk chemical composition of studied samples from Kara Sea (XRF data; wt. %).

No	Sample	SiO_2	Al_2O_3	TiO_2	Fe_2O_{3tot}	MnO_{tot}	Mn/Fe	MgO	CaO	Na_2O	K_2O	P_2O_5	LOI
1	FN-23-k	32.99	4.81	0.35	20.02	16.00	0.89	2.58	2.27	2.42	1.33	2.42	15.0
2	FN-69-k	51.88	4.85	0.17	18.65	5.74	0.34	1.96	1.46	1.83	1.33	2.18	10.4
3	FN-50-k	33.66	4.87	0.32	15.06	20.57	1.51	2.83	2.44	2.08	1.33	2.00	15.0
4	FN-77-k2	43.02	4.97	0.23	15.71	13.57	0.96	2.31	1.70	2.22	1.40	2.14	13.0
5	FN-54-k1	26.47	4.73	0.29	15.08	26.55	1.95	2.98	2.09	2.49	1.25	1.88	16.3
6	FN-56-k1	37.60	5.68	0.32	10.08	23.64	2.60	2.61	1.92	2.55	1.50	1.23	13.0
7	FN-46-k2	19.36	4.38	0.26	10.59	30.55	3.19	2.83	2.29	2.81	1.21	1.19	24.5
8	FN-147-k2	27.26	5.16	0.33	17.62	23.41	1.47	2.71	1.81	2.31	1.46	2.08	16.0
9	H-138-k	46.64	8.81	0.28	17.59	6.69	0.42	2.08	1.77	2.83	2.03	1.78	9.9
10	H-189-k	41.51	7.51	0.46	29.79	2.57	0.10	2.24	0.87	1.64	1.62	1.57	10.6
11	H-21-k	29.59	6.67	0.36	16.83	23.98	1.58	2.42	1.66	2.99	1.53	1.80	12.3
12	H-16-k	22.82	5.20	0.35	14.11	32.93	2.58	2.40	1.89	3.18	1.44	1.77	13.7
13	H-226-k,t	26.74	6.47	0.31	18.52	25.18	1.51	2.18	1.71	3.34	1.50	1.45	12.7
14	H-101-k	28.67	5.84	0.30	13.69	29.18	2.36	1.95	1.66	3.32	1.54	1.23	12.5
15	H-41-k	32.78	6.88	0.34	23.67	15.68	0.73	2.04	1.36	3.10	1.56	1.73	11.2
16	H-65-k	35.55	5.55	0.34	23.09	15.52	0.74	1.83	1.57	2.78	1.41	1.87	10.7

Table 4
Geochemical data for samples from Kara Sea (ICP-MS data; ppm).

No	Sample	Co	Ni	Cu	Mo	V	Cr	Rb	Sr	Nb	Y	Zr
1	FN-23-k	132	128	19	252	271	14	25	462	3.77	24	38
2	FN-69-k	75	63	18	43	251	18	24	346	1.96	27	30
3	FN-50-k	107	80	29	90	210	20	22	605	1.73	27	26
4	FN-77-k2	73	79	29	100	208	13	25	403	2.68	27	31
5	FN-54-k1	132	111	43	58	183	14	23	619	< 0.5	31	13
6	FN-56-k1	75	101	40	114	186	16	28	493	0.70	26	27
7	FN-46-k2	87	230	51	313	221	14	19	419	1.23	20	23
8	FN-147-k2	142	151	46	183	238	21	23	509	3.29	26	34
9	H-138-k	90	63	15	35	179	5	40	455	4.09	18	40
10	H-189-k	68	68	12	51	304	45	40	179	5.09	20	58
11	H-21-k	105	131	70	149	236	25	35	495	3.24	22	72
12	H-16-k	104	104	52	209	246	25	26	487	2.99	20	50
13	H-226-k,t	91.4	179	50	264	342	26	30	340	3.75	18	56
14	H-101-k	118	221	30	278	296	29	30	370	3.54	16	100
15	H-41-k	130	119	68	110	514	35	32	349	3.67	27	66
16	H-65-k	118	130	47	136	296	27	28	377	3.50	24	128

No	Sample	La	Ce	Pr	Nd	Sm	Eu	Gd	Tb	Dy	Ho
1	FN-23-k	19.1	28.9	4.44	18.2	3.98	1.01	4.55	0.75	4.48	0.97
2	FN-69-k	20.5	29.3	4.70	19.3	4.35	1.16	5.06	0.83	5.01	1.06
3	FN-50-k	21.0	33.7	4.87	20.1	4.47	1.12	4.99	0.82	4.89	1.05
4	FN-77-k2	20.5	31.8	4.71	19.7	4.38	1.11	4.84	0.80	4.76	1.02
5	FN-54-k1	24.6	44.7	5.80	23.6	5.22	1.35	5.95	0.99	5.85	1.24
6	FN-56-k1	25.1	47.6	5.94	23.8	5.09	1.22	5.34	0.85	4.85	1.02
7	FN-46-k2	15.4	22.9	3.61	14.8	3.33	0.85	3.79	0.63	3.73	0.81
8	FN-147-k2	20.7	32.8	4.79	19.7	4.43	1.12	5.02	0.83	4.91	1.06
9	H-138-k	20.0	33.9	4.46	17.3	3.50	0.97	3.68	0.61	3.44	0.72
10	H-189-k	21.9	43.0	5.22	20.4	4.26	1.02	4.34	0.71	4.08	0.86
11	H-21-k	20.5	32.7	4.27	18.1	4.00	0.92	4.12	0.60	3.68	0.72
12	H-16-k	18.2	30.8	3.81	16.2	3.90	1.00	4.00	0.55	3.57	0.70
13	H-226-k,t	19.1	31.2	4.15	17.1	4.00	0.83	3.85	0.54	3.38	0.71
14	H-101-k	16.3	28.2	3.49	15.2	3.28	0.81	3.42	0.48	2.82	0.57
15	H-41-k	24.5	34.5	5.10	21.7	4.89	1.13	5.27	0.74	4.65	0.87
16	H-65-k	27.7	46.5	5.73	24.4	5.00	0.98	5.08	0.72	4.18	0.84

No	Sample	Er	Tm	Yb	Lu	Hf	Ta	Th	U	Ce/Ce*	Y_{PAAS}/Ho_{PAAS}
1	FN-23-k	2.72	0.37	2.44	0.36	1.01	0.29	2.29	3.30	0.7	0.9
2	FN-69-k	2.90	0.41	2.65	0.39	0.73	0.16	1.85	2.94	0.7	0.9
3	FN-50-k	2.85	0.41	2.61	0.40	0.73	< 0.1	2.08	4.87	0.8	0.9
4	FN-77-k2	2.85	0.40	2.58	0.38	0.91	0.22	2.10	3.67	0.7	1.0
5	FN-54-k1	3.39	0.48	3.10	0.46	0.62	< 0.1	1.99	6.44	0.9	0.9
6	FN-56-k1	2.72	0.38	2.49	0.38	0.81	< 0.1	3.10	4.21	0.9	0.9
7	FN-46-k2	2.21	0.31	2.03	0.31	0.63	< 0.1	1.70	5.14	0.7	0.9
8	FN-147-k2	2.94	0.42	2.74	0.45	0.95	0.30	2.43	6.05	0.8	0.9
9	H-138-k	2.00	0.28	1.86	0.28	1.06	0.37	3.00	4.98	0.8	0.9
10	H-189-k	2.32	0.34	2.22	0.37	1.51	0.36	4.05	5.67	0.9	0.9
11	H-21-k	2.06	0.27	1.80	0.29	2.08	0.29	3.38	6.06	0.8	1.1
12	H-16-k	1.96	0.27	1.52	0.28	1.37	0.21	2.30	5.34	0.9	1.0
13	H-226-k,t	1.92	0.24	1.71	0.22	1.22	0.27	2.80	3.89	0.8	0.9
14	H-101-k	1.53	0.23	1.56	0.22	2.59	0.29	2.46	4.33	0.9	1.0
15	H-41-k	2.60	0.40	2.40	0.35	1.65	0.28	2.78	4.56	0.7	1.1
16	H-65-k	2.32	0.32	2.29	0.32	3.38	0.34	6.51	3.04	0.9	1.1

Note: $Ce/Ce^* = \frac{Ce_{PAAS}}{\sqrt{La_{PAAS} * Pr_{PAAS}}}$, where Ce_{PAAS}, La_{PAAS} and Pr_{PAAS} are normalized to *PAAS* values.

The Fe-P-rich layers are almost completely composed of an amorphous phase under X-ray, with only one sample containing trace amounts of goethite. No phosphates were detected. Despite the high phosphorus content (> > 0.5 wt%; Table 2), the studied Fe-Mn nodules from the Kara Sea are characterized by negative Ce and Y anomalies (Fig. 8), which might indicate the absence of the phosphorization process and/or several sources (i.e., marine and fluvial) of sediment matter during formation of the concretions. Probably, P_2O_5 contents of the Kara Sea concretions was taken up during the primary formation of the Fe-rich phases.

According to Bau et al. (2014) the diagenetic Fe–Mn nodules display negative Y anomalies and negative Ce anomalies, while hydrogenetic crusts and nodules show negative Y anomalies and positive Ce anomalies. Ferro-manganese nodules from the Kara Sea show negative Y anomalies and negative Ce anomalies (Fig. 8), which could be the geochemical signature of their diagenetic origin. Ferro-manganese nodules from the Kara Sea also show chemical features of diagenetic type of concretions according to Ce/Ce* ratio *vs* Nd concentration plot (Fig. 9) proposed by Bau et al. (2014).

However, Mn/Fe ratios of ferro-manganese nodules from the Kara Sea is ≤5, which is according to Halbach and Puteanus (1988) could be a signature of hydrogenetic process.

Based on the above (geological settings, growth rate, mineralogical, textural and chemical features) we can assume that ferro-manganese nodules from the Kara Sea were formed mainly by diagenetic process, while hydrogenetic process is auxiliary if present.

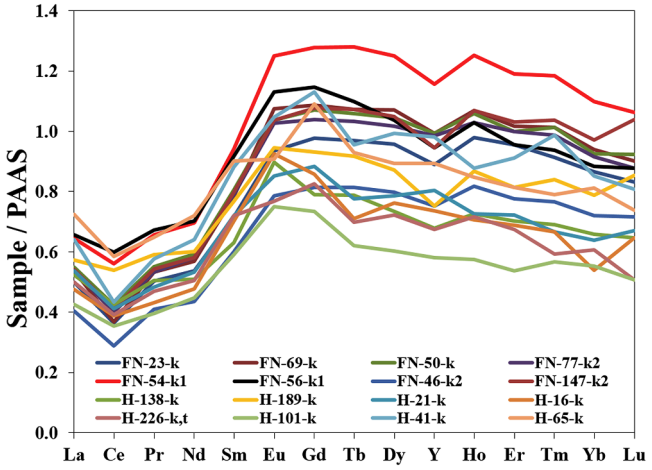

Fig. 8. REY_{SN} patterns of Fe-Mn nodules of Kara Sea.

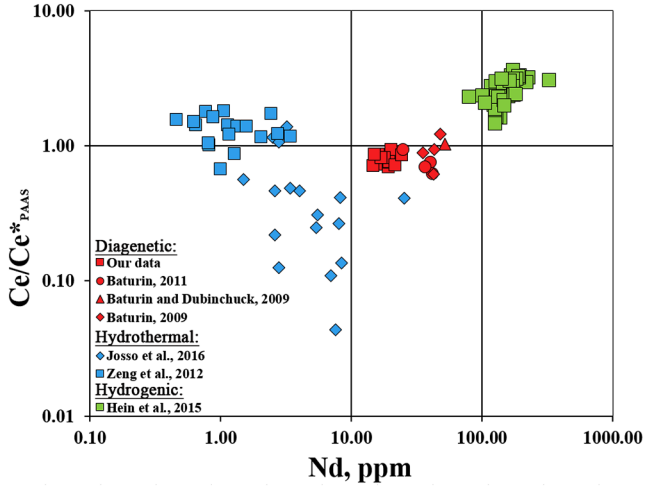

Fig. 9. Different genetic types of Fe–Mn crusts and nodules in Ce/Ce* ratio *vs* Nd concentration (after Bau et al., 2014).

5.2. Relation to other types of Fe-Mn concretions

There are a wide variety of methods to date which allow us to classify Fe-Mn concretions based on their chemical composition (e.g. Bonatti et al., 1972, Bau et al., 2014, Josso et al., 2017). Commonly used ternary diagrams (e.g. Fe – Mn – (Cu + Ni + Co) × 10, Fe – Mn – Co × 100 (e.g. Bonatti et al., 1972; Toth, 1980; Usui and Nishimura, 1992; Prakash et al., 2012)) does not clearly discriminate Fe-Mn deposits formed by mixed genetic processes such as nodules with various hydrogenetic/diagenetic proportions, hydrothermally derived particles incorporated during hydrogenetic crust growth, and some hydrothermal samples (e.g. Josso et al., 2017). Accurate determination of the concentrations of Ce (Ce, Ce/Ce*), Y, Ho, Nd and Zr has become the main tool for elucidating the genesis of nodules and crusts (Bau et al., 2014, Josso et al., 2017).

To identify similarities and differences, we selected several typical examples of diagenetic (Baturin, 2009; Baturin, 2011; Baturin and Dubinchuk, 2009), hydrogenetic (Hein et al., 2015), and hydrothermal Fe-Mn crusts and nodules (Zeng et al., 2012; Josso et al, 2017).

Fe-Mn nodules from the Kara Sea (our data; Baturin, 2011), along with concretions from the Gulf of Riga (Baturin and Dubinchuk, 2009) and the Gulf of Finland (Baturin, 2009), plot in the field of diagenetic concretions on the diagram (Fig. 9) proposed by Bau et al. (2014). All diagenetic Fe-Mn crusts and nodules form a common group, characterized by a Ce/Ce* ratio of < 1 (0.7–0.9) and an Nd content of > 10

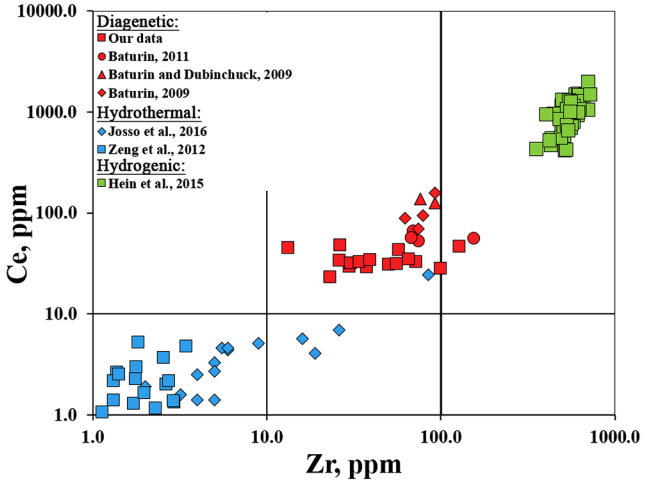

Fig. 10. Different genetic types of Fe–Mn crusts and nodules in graphs of Ce concentration *vs* Zr concentration.

(17–24 ppm). Diagenetic Fe-Mn crusts and nodules (our data, Baturin, 2009; Baturin, 2011; Baturin and Dubinchuk, 2009) differ greatly from the high-temperature hydrothermal Fe-Mn crusts and nodules from the PACMANUS hydrothermal field, Eastern Manus Basin (Ce/Ce* ratio of 0.7–1.8; Nd content of 0.5–3.5; Zeng et al., 2012), low-temperature hydrothermal Fe-Mn crusts and nodules from Wallis and Futuna (Ce/Ce* ratio of 0.1–1.4, Nd content of 1.5–25.3; Josso et al, 2017), as well as hydrogenetic Fe-Mn crusts and nodules from the Cook Islands EEZ (Ce/Ce* ratio of 1.5–3.3; Nd content of 79.3–323.0; Hein et al., 2015).

Since trace element contents in diagenetic concretions (our data; Baturin, 2009; Baturin and Dubinchuk, 2009; Baturin, 2011) are low (which is probably caused by dilution of detrital material) we suggest to use not only element content (Figs. 10 and 11), but also elemental ratios (Fig. 12) to distinguish different genetic types of concretions.

If we assume that the source of aluminum in the concretions was only terrigenous material, then one can estimate the degree of enrichment of concretions with certain elements relative to the background detrital substance ($C_i^N = (C_i/C_{Al})_{sample}/(C_i/C_{Al})_{shale}$; Li and Schoonmaker, 2003).

On the Zr *vs* Ce diagram (Fig. 10), the diagenetic nodules (our data, Baturin, 2009, Baturin, 2011, Baturin and Dubinchuk, 2009) are characterized by Zr and Ce contents of 13–156 and 29–157 ppm, respectively. Hydrothermal nodules (Zeng et al., 2012; Josso et al, 2017) are characterized by low Zr (< 25 ppm) and Ce (< 10 ppm) contents.

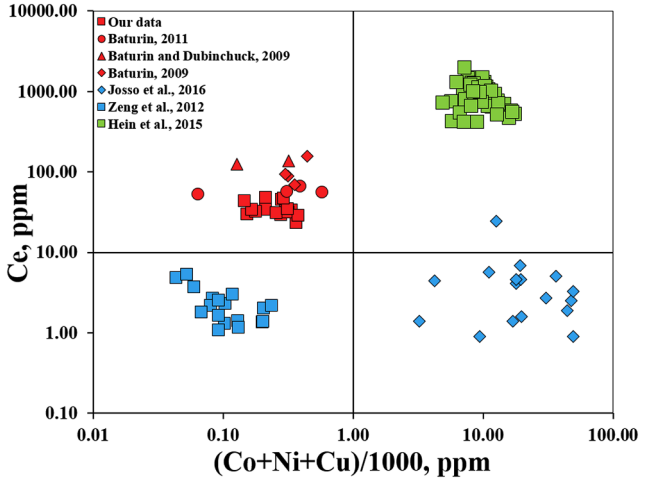

Fig. 11. Different genetic types of Fe–Mn crusts and nodules in graphs of Ce concentration *vs* (Co + Ni + Cu)/1000 ratio.

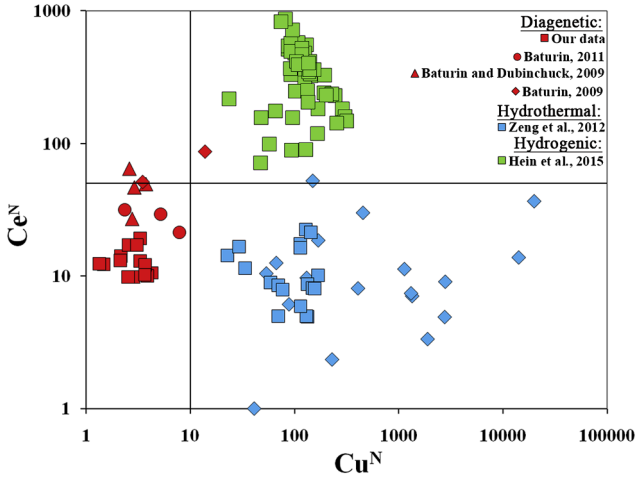

Fig. 12. Different genetic types of Fe–Mn crusts and nodules in graphs of Ce^N concentration *vs* Cu^N ratio. Note: $Ce^N = (C_{Ce}/C_{Al})_{sample}/(C_{Ce}/C_{Al})_{shale}$; $Cu^N = (C_{Cu}/C_{Al})_{sample}/(C_{Cu}/C_{Al})_{shale}$.

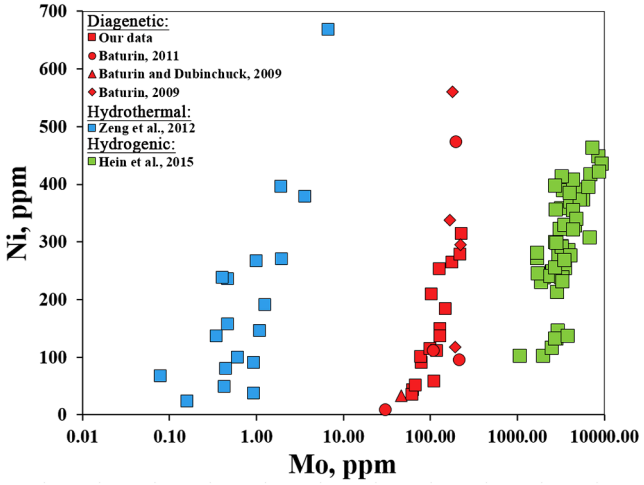

Fig. 13. Different genetic types of Fe–Mn crusts and nodules in graphs of Ni concentration *vs* Mo concentration.

One sample from Josso et al, (2017) falls into the field of digenetic Fe-Mn crusts and nodules, which may be due to the mixed nature of the nodules studied by the authors. High Zr (> 350 ppm) and Ce (> 420 ppm) contents characterize hydrogenetic concretions (Hein et al., 2015).

On the ((Co + Ni + Cu)/1000 *vs* Ce diagram (Fig. 11), diagenetic concretions (our data, Baturin, 2009, Baturin, 2011, Baturin and Dubinchuk, 2009) are characterized by low Co, Ni and Cu contents ((Co + Ni + Cu)/1000 < 1) and a high (> 10 ppm) Ce content. Hydrogenetic concretions (Hein et al., 2015) are characterized by high Co, Ni and Cu contents ((Co + Ni + Cu)/1000 > 1) and a high (> 10 ppm) Ce content. High-temperature and low-temperature hydrothermal concretions have different chemical features. High-temperature hydrothermal concretions (Zeng et al., 2012) are characterized by low Co, Ni and Cu contents ((Co + Ni + Cu)/1000 < 1) and a low (< 10 ppm) Ce content. By contrast, low-temperature hydrothermal concretions (Josso et al., 2017) are characterized by high Co, Ni, and Cu contents ((Co + Ni + Cu)/1000 > 1) and a low (< 10 ppm) Ce content.

Elemental ratios also shows that diagenetic concretions are differ from other genetic types of concretions. On the Cu^N *vs* Ce^N diagram (Fig. 12), diagenetic concretions (our data, Baturin, 2009; Baturin, 2011; Baturin and Dubinchuk, 2009) are characterized by relatively low Cu contents (Cu^N < 10) and a Ce content (Ce^N < 50). Hydrogenetic concretions (Hein et al., 2015) are characterized by relatively high Cu contents (Cu^N > 10) and a Ce content (Ce^N > 50). Diagenetic and hydrogetic concretions form separate point cloud, only one sample (Baturin, 2009) show intermediate value, which could be a sign of its mixed nature. High-temperature and low-temperature hydrothermal concretions are characterized by relatively high Cu contents (Cu^N > 10) and a relatively low Ce content (Ce^N < 50).

The different genetic types of nodules also differ in their Mo content (Fig. 13), which varies by more than 4 orders of magnitude. High-temperature hydrothermal concretions (Zeng et al., 2012) are characterized by the lowest Mo content (< 1 ppm), diagenetic concretions (our data, Baturin, 2009; Baturin, 2011; Baturin and Dubinchuk, 2009) by an intermediate Mo content (~50 to 150 ppm), and hydrogenetic concretions (Hein et al., 2015) by the highest Mo content (> 1000 ppm).

We can draw the following conclusions based on our comparison of the Fe-Mn concretions of the Kara Sea with other diagenetic Fe-Mn concretions, and also with hydrogenetic and hydrothermal Fe-Mn concretions. Firstly, all considered diagenetic concretions have a similar chemical composition that characterizes comparable formation conditions. Secondly, the considered diagenetic concretions have a significantly different chemical composition to the hydrogenetic and hydrothermal concretions, allowing the three groups of Fe-Mn concretions to be differentiated based on a study of their chemical composition. Lastly, diagenetic crusts and nodules can be identified by their Co, Ni, Cu, Ce, Zr and Mo contents.

6. Conclusions

Fe-Mn concretions from the Kara Sea were studied by optical and scanning electron microscopy, X-ray powder diffraction, X-ray fluorescence analysis, inductively coupled plasma mass spectrometry, and electron microprobe analysis.

The geological setting, mineralogy and geochemistry of ferro-manganese nodules from the Kara Sea show that they were formed mainly by diagenetic process, while hydrogenetic process is auxiliary if present.

All studied nodules have similar contents of the main chemical elements, except for variability in the Mn/Fe ratio and silica content, and contain a significant amount of phosphorus (> 1 wt% P_2O_5).

The content of rare-earth elements for all studied samples is comparable and does not exceed 160 ppm. PAAS-normalized rare earth element contents in the nodules suggest a similar geochemical origin. In all cases, the samples are depleted in light REE, enriched in heavy REE, and strong negative Ce and Y anomalies were observed.

The studied nodules are characterized by the alternation of Mn- and Fe-P-enriched laminae. The Fe-P-rich laminae are almost completely composed of an amorphous phase under X-ray, with only one sample containing trace amounts of goethite. The P_2O_5 contents, an absence of crystalline P phases and absence of Ca-P correlation indicate that P is bound to the Fe (hydro)oxide phase and the P enrichment thus is a primary process during the Fe oxide formation.

In all cases, the manganese-containing phases (10-Å and 7-Å) are destroyed at a temperature range of 350–550 °C during lab experiments, which unequivocally indicates the absence of todorokite (Bish and Post, 1989; Post et al., 2003). At least two different Mn-bearing phases, which differ in morphology and chemical composition, are present in the studied samples. Based on our data, the Mn-rich laminae are predominantly composed of crystalline phases (buserite-1, birnessite) and, to a lesser extent, by the phase which is amorphous under X-ray. Quartz, albite, and feldspars (microcline and plagioclase) were found in all samples. Clays are composed of Mg-Fe-rich chlorite, smectite, kaolinite and Mg-Fe-rich mica. Ilmenite, monazite, zircon, rutile, epidote, Mg-Fe-rich amphibole and chromite were found in subordinate quantities.

Our data indicate that diagenetic crusts and nodules differ significantly in terms of chemical composition from the other types of Fe-Mn concretions. Based on their Co, Ni and Cu, Ce, Zr and Mo contents, we could differentiate diagenetic concretions from hydrogenetic and hydrothermal (both high and low-temperature) concretions.

Acknowledgements

This work was supported by the Russian Science Foundation Grant № 17-17-01171. J. Barnet improved English and provided useful comments. Discussion with N. Konstantinova, G. Cherkashov, A. Krylov and comments of an anonymous reviewer greatly improved the manuscript.

References

Anikeeva, L., Andreev, S., Kazakova, V., Aleksandrov, P., Zadornov, M., Kuznetsov, V., Petuchov, S., Kulikov, N., Torochov, M., Chernomordik, A., Burskiy, A., 2002. Cobalt-rich ores of World Ocean. VNIIOkeangeologia, St. Petersburg (in Russian with English abstract).

Aplin, A.C., Cronan, D.S., 1985. Ferromanganese oxide deposits from the central Pacific Ocean, II. Nodules and associated sediments. Geochim. Cosmochim. Acta 49, 437–451.

Asavin, A.M., Kubrakova, I.V., Mel'nikov, M.E., Tyutyunnik, O.A., Chesalova, E.I., 2010. Geochemical Zoning in Ferromanganese crusts of ItaMaiTai Guyot. Geochem. Int. 48 (5), 423–445.

Baturin, G.N., 1988. In: The Geochemistry of Manganese and Manganese Nodules in the Ocean. Springer, Netherlands, pp. 356.

Baturin, G.N., 2009. Geochemistry of ferromanganese nodules in the Gulf of Finland, Baltic Sea. Lith. Miner. Resour. 44 (5), 411–426.

Baturin, G.N., Dubinchuk, V.T., 2009. Composition of ferromanganese nodules from Riga Bay (Baltic Sea). Oceanology 49 (1), 111–120.

Baturin, G.N., 2011. Variations in the composition of ferromanganese concretions of the Kara Sea. Okeanologiya 51 (1), 153–161 (in Russian).

Baturin, G.N., Dubinchuk, V.T., Rashidov, V.A., 2011. Distribution of microelements in ferromanganese crusts of the sea of Okhotsk. Doklady Earth Sci. 440 (1), 1291–1297.

Bau, M., Koschinsky, A., Dulski, P., Hein, J.R., 1996. Comparison of the partitioning behaviours of yttrium, rare earth elements, and titanium between hydrogenetic marine ferromanganese crusts and seawater. Geochim. Cosmochim. Acta 60, 1709–1725.

Bau, M., Schmidt, K., Koschinsky, A., Hein, J.R., Usui, A., 2014. Discriminating between different genetic types of marine ferro-manganese crusts and nodules based on rare earth elements and yttrium. Chem. Geol. 381, 1–9.

Bilinski, H., Giovanoli, R., Usui, A., Hanzel, D., 2002. Characterization of Mn oxides in cemented streambed crusts from Pinal Creek, Arizona, U.S.A., and in hot-spring deposits from Yuno-Taki Falls, Hokkaido, Japan. Am. Mineral. 87, 580–591.

Bish, D.L., Post, J.E., 1989. Thermal behavior of complex, tunnel-structure manganese oxides. Am. Mineral. 74, 177–186.

Bogdanov, Yu.A., Gorshkov, A.I., Gurvich, E.G., Bogdanova, O.Yu., Dubina, G.I., Ivanov, G.V., Isaeva, A.B., Muravev, K.G., 1994. Iron-manganese concretions of the Kara Sea. Okeanologiya 34 (5), 789–800 (in Russian).

Bonatti, E., 1975. Metallogenesis at oceanic spreading centers. Annu. Rev. Earth Planet. Sci. 3, 401–431.

Bonatti, E., Kraemer, T., Rydell, H., 1972. Classification and genesis of submarine iron–manganese deposits. In: Horn, D.R. (Ed.), Papers from a Conference on Ferromanganese Deposits on the Ocean Floor. Natl. Sci. Found., pp. 149–166.

Burns, V.M., Burns, R.G., 1978. Authigenic todorokite and phillipsite inside deep sea manganese nodules. Am. Mineral. 63, 827–831.

Calvert, S.E., Price, N.B., 1977. Geochemical variation in ferromanganese nodules and associated sediments from the Pacific Ocean. Mar. Chem. 5, 43–74.

Cherkashov, G., Kuznetsov, V., Kuksa, K., Tabuns, E., Maksimov, F., Bel'tenev, V., 2017. Sulfide geochronology along the Northern Equatorial Mid Atlantic Ridge. Ore Geol. Rev. 87, 147–154.

Chukhrov, F.V., Gorshkov, A.I., Drits, V.A., 1989. In: Supergenic Manganese Hydrous Oxides. Nauka, Moscow, pp. 208.

Chukhrov, F.V., Zvyagin, B.B., Yermilova, L.P., Gorshkov, A.I., 1976. Mineralogical criteria in the origin of marine iron-manganese nodules. Mineral. Deposita 11, 24–32.

Crerar, D.A., Barnes, H.Z., 1974. Deposition of deep-sea manganese nodules. Geochim. Cosmochim. Acta 38 (2), 279–300.

Drachev, S.S., 2016. Fold belts and sedimentary basins of the Eurasian Arctic. Arktos 2, 21.

Drits, V.A., Silvester, E., Gorshkov, A.I., Manceau, A., 1997. The structure of syntheticmonoclinic Na-rich birnessite and hexagonal birnessite. Part 1. Results from X-ray diffraction and selected area electron diffraction. Am. Mineral. 82, 946–961.

Emelyanov, E.M., 2005. In: 2005 The Barrier Zones in the Ocean. Springer-Verlag, Berlin Heidelberg, pp. 632.

Ershova, V.B., Prokopiev, A.V., Khudoley, A.K., Shneider, G.V., Andersen, T., Kallerund, K., Makariev, A.A., Kolchanov, D.A., 2015. U-Pb dating of detrital zircons from the Lower Paleozoic deposits of the North Kara basin. Doklady Earth Sci. 464 (4), 444–447.

Gurevich, V.I., Yakovlev, A.V., 1993. Fero-manganees crusts and concretions of the Kara Sea. Cobalt-bearing ferromanganese crusts of the Pacific Ocean. VNIIOkeangeologiya 97–111 (in Russian).

Faleide, J.I., Pease, V., Curtis, M., Klitzke, P., Minakov, A., Scheck-Wenderoth, M., Kostyuchenko, S., Zayonchek, A., 2017. Tectonic implications of the lithospheric structure across the Barents and Kara shelves. In: Pease, V., Coakley, B. (eds) 2018. Circum-Arctic Lithosphere Evolution. Geol. Soc., London, Spec. Publ. 460, 285–314.

Falkner, K.K., Steele, M., Woodgate, R.A., Swift, J.H., Aagaard, K., Morison, J., 2004. Dissolved oxygen extrema in the Arctic Ocean halocline from the North Pole to the Lincoln Sea. Revised for Deep-Sea Research, p. 34.

González, F.J., Somoza, L., Leon, R., Medialdea, T., de Torres, T., Ortiz, J.E., Lunar, R., Martinez-Frias, J., Merinero, R., 2012. Ferromanganese nodules and micro-hardgrounds associated with the CadizContourite Channel (NE Atlantic): palaeoenvironmental records of fluid venting and bottomcurrents. Chem. Geol. 310–311, 56–78.

Halbach, P., Puteanus, D., 1988. Geochemical trends of different genetic types of nodules and crusts. In: Halbach, P., Friedrich, G., Von Stackelberg, U. (Eds.), The Manganese Nodule Belt of the Pacific Ocean. Ferdinand Enke, Stuttgart, pp. 61–69 (Chapter 4).

Hein, J.R., Schulz, M.S., Dunham, R.E., Stern, R.J., Bloomer, S.H., 2008a. Diffuse flow hydrothermal manganese mineralization along the active Mariana and southern Izu-Bonin arc system, western Pacific. J. Geophys. Res. 113 (BO8S14, 29pp.).

Hein, J.R., Mizell, K., Koschinsky, A., Conrad, T.A., 2013. Deep-ocean mineral deposits as a source of critical metals for high- andgreen-technology applications: comparison with land-based resources. Ore Geol. Rev. 51, 1–14.

Hein, J.R., Koschinsky, A., 2013. Deep-ocean ferromanganese crusts and nodules. In: Holland, H.D., Turekian, K.K. (Eds.), 2nd Ed. Treatise on Geochemistry vol. 13. Elsevier, Amsterdam, pp. 273–291 (Chapter 11).

Hein, J.R., Koschinsky, A., Halbach, P., Manheim, F.T., Bau, M., Kang, J.-K., Lubik, N., 1997. Iron and manganese oxide mineralization in the Pacific. In: Nicholson, K., Hein, J.R., Bühn, B., Dasgupta, S. (Eds.), Manganese Mineralization: Geochemistry and Mineralogy of Terrestrial and Marine Deposits. pp. 123–138.

Hein, J.R., Schulz, M.S., Dunham, R.E., Stern, R.J., Bloomer, S.H., 2008b. Diffuse flow hydrothermal manganese mineralization along the active Mariana and southern Izu-Bonin arc system, western. Pacific. J. Geophys. Res. 113 (8), 1–29.

Hein, J.R., Spinardi, F., Okamoto, N., Mizell, K., Thorburn, D., Tawake, A., 2015. Critical metals in manganese nodules from the Cook Islands EEZ, abundances and distributions. Ore Geol. Rev. 68, 97–116.

Hörner, T., Stein, R., Fahl, K., 2018. Paleo-sea ice distribution and polynya variability on the Kara Sea shelf during the last 12 ka. Arktos 4 (6) 16 p.

Josso, P., Pelleter, E., Pourret, O., Fouquet, Y., Etoubleaua, J., Cheron, S., Bollinger, C., 2017. A new discrimination scheme for oceanic ferromanganese deposits using high field strength and rare earth elements. Ore Geol. Rev. 87, 3–15.

Konstantinova, N., Cherkashov, G., Hein, J.R., Mirão, J., Dias, L., Madureira, P., Kuznetsov, V., Maksimov, F., 2017. Composition and characteristics of the ferromanganese crusts from the western Arctic Ocean. Ore Geol. Rev. 87, 88–99.

Khudoley, A.K., Verzhbitsky, V.E., Zastrozhnov, D.A., O'Sullivan, P., Ershova, V.B., Proskurnin, V.F., Tuchkova, M.I., Rogov, M.A., Kyser, T.K., Malyshev, S.V., Schneider, G.V., 2018. Late Paleozoic – Mesozoic tectonic evolution of the eastern Taimyr-Severnaya Zemlya Fold and Thrust Belt and adjoining Yenisey-Khatanga Depression. J. Geodyn. 119, 221–241. https://doi.org/10.1016/j.jog.2018.02.002.

Koshelev, B.A., 1984. Iron-manganese nodules of the Kara Sea. Tr. Arctic. Antarctic. Sci. Inst. 368, 119–127.

Koschinsky, A., Halbach, P., 1995. Sequential leaching of marine ferromanganese precipitates: genetic implications. Geochim. Cosmochim. Acta 59, 5113–5132.

Koschinsky, A., Hein, J.R., 2003. Uptake of elements from seawater by ferromanganese crusts: solid-phase associations and seawater speciation. Mar. Geol. 198, 331–351.

Kuhn, T., Wegorzewski, A., Rühlemann, C., Vink, A., 2017. Composition, formation, and occurrence of polymetallic nodules. In: Sharma R. (Eds.) Deep-Sea Mining: Resource Potential, Technical and Environmental Considerations. pp. 23–63.

Lei, G., Boström, K., 1995. Mineralogical control on transition metal distributions in marine manganese nodules. Mar. Geol. 23 (3–4), 253–261.

Levitan, M.A., Bourtman, M.V., Demina, L.L., Krupskaya, V.V., Sedykh, E.M., Chudetsky, M.Yu., 2004. History of Holocene sedimentation in the Southern Kara Sea. Lithol. Mineral Resour. 39, 566–579.

Li, Y.H., Schoonmaker, J.E., 2003. Chemical composition and mineralogy of marine sediments. In: In: Mackenzie, F.T. (Ed.), Sediments, Diagenesis, and Sedimentary Rocks – Treatise on Geochemistry Vol. 7. Elsevier, Amsterdam, pp. 1–35.

Lisitsin, A.P., Kharin, G.S., Chernysheva, E.A., 2004. Coarse ice-rafted debris in the bottom sediments of the Kara Sea. Oceanology 44, 412–427.

Makariev, A.A. (Ed.), 2012. State Geological Map of the Russian Federation. Scale 1:1 000 000 (third generation). Sheet T-45 – 48th. Cheliuskin. VSEGEI publishing, St. Petersburg.

Manceau, A., Drits, V.A., Silvester, E., Bartoli, C., Lanson, B., 1997. Structural mechanism of Co_2 oxidation by the phyllomanganate buserite. Am. Mineral. 82, 1150–1175.

Morozov, A.F., Petrov, O.V., 2004. State Geological Map of the Russian Federation. Scale 1: 2500 000. VSEGEI Publishing House, St. Petersburg (in Russian).

Muiños, S.B., Hein, J.R., Frank, M., Monteiro, J.H., Gaspar, L., Conrad, T., Pereira, H.G., Abrantes, F., 2013. Deep-sea Fe-Mn crusts from the Northeast Atlantic Ocean: composition and resource considerations. Mar. Geores. Geotechnol. 31 (1), 40–70.

Nordenskjold, A.E., 1881. In: The Voyage of the Vega Round Asia and Europe. L. Macmillan, pp. 521.

Pease, V., Drachev, S., Stephenson, R., Zhang, X., 2014. Arctic lithosphere – a review. Tectonophysics 625, 1–25.

Polyak, L., Levitan, M., Khusid, T., Merklin, L., Mukhina, V., 2002. Variations in the influence of riverine discharge on the Kara Sea during the last deglaciation and the Holocene. Global Planet. Change 32, 291–309.

Post, J.E., Heaney, P.J., Hanson, J., 2003. Synchrotron X-ray diffraction study of the structure and dehydration behavior of todorokite. Am. Mineral. 88, 142–150.

Prakash, L.S., Ray, D., Paropkari, A.L., Mudholkar, A.V., Satyanarayanan, M., Sreenivas, B., Chandrasekharam, D., Kota, D., Raju, K.A.K., Kaisary, S., Balaram, V., Gurav, T., 2012. Distribution of REEs and yttrium among major geochemical phases of marine Fe–Mn-oxides: Comparative study between hydrogenous and hydrothermal deposits. Chem. Geol. 312–313, 127–137.

Rozanov, A.G., 2015. Redox System of the bottom sediments of the western Kara Sea. Geochem. Int. 53, 987–1001.

Rusakov, V.Yu., Kuzhmina, T.G., Levitan, M.A., Toropchenova, E.S., Zhylkina, A.V., 2017. Lithological and geochemical typification of surface bottom sediments in the Kara Sea. Oceanology 57, 192–203.

Stein, R., Dittmers, K., Fahl, K., Kraus, M., Matthiessen, J., Niessen, F., Pirrung, M., Polyakova, Ye, Schoster, F., Steinke, T., Fütterer, D.K., 2004. Arctic (palaeo) river discharge and environmental change: evidence from the Holocene Kara Sea sedimentary record. Quat. Sci. Rev. 23, 1485–1511.

Taylor, S.R., McLennan, S.M., 1985. In: The Continental Crust: Its Composition and Evolution. Blackwell Scientific Publication, Carlton, pp. 312.

Toth, J.R., 1980. Deposition of submarine crusts rich in manganese and iron. Bull. Geol. Soc. Am. 91, 44–54.

Usui, A., Nishimura, A., 1992. Hydrothermal manganese deposits from the Izu-Ogasawara (Bonin)-Mariana Arc and adjacent areas. Bull. Geol. Surv. Jpn. 43, 257–284.

von Stackelberg, U., 1997. Growth history of manganese nodules and crusts of the Peru Basin. Geol. Soc., London, Spec. Publ. 119, 153–176.

von Stackelberg, U., 2000. Manganese nodules of the Peru Basin. In: Cronan, D.S. (Ed.), Handbook of Marine Mineral Deposits. CRC Press, Boca Raton, Florida, pp. 197–238.

Wegorzewski, A.V., Kuhn, T., Dohrmann, R., Wirth, R., Grangeon, S., 2015. Mineralogical characterization of individual growth structures of Mn-nodules with different Ni + Cu content from the central Pacific Ocean. Am. Mineral. 100, 2497–2508.

Zeng, Z., Ouyang, H., Yin, X., Chen, S., Wang, X., Wua, L., 2012. Formation of Fe–Si–Mn oxyhydroxides at the PACMANUS hydrothermal field, Eastern Manus Basin: mineralogical and geochemical evidence. J. Asian Earth Sci. 60, 130–146.